Article

# Electronic origin of high superconducting critical temperature in trilayer cuprates

Xiangyu Luo[1,2,8], Hao Chen[1,2,8], Yinghao Li[1,2,8], Qiang Gao[1], Chaohui Yin[1,2], Hongtao Yan[1,2], Taimin Miao[1,2], Hailan Luo [1,2], Yingjie Shu[1,2], Yiwen Chen[1,2], Chengtian Lin[3], Shenjin Zhang[4], Zhimin Wang[4], Fengfeng Zhang[4], Feng Yang[4], Qinjun Peng[4], Guodong Liu[1,2,5], Lin Zhao [1,2,5], Zuyan Xu[4], Tao Xiang [2,5,6,7] & X. J. Zhou [1,2,5,7] ✉

In high-temperature cuprate superconductors, the superconducting transition temperature ($T_c$) depends on the number of $CuO_2$ planes in the structural unit and the maximum $T_c$ is realized in the trilayer system. Trilayer superconductors also exhibit an unusual phase diagram where $T_c$ is roughly constant in the overdoped region, which is in contrast to the decrease usually found in other cuprate superconductors. The mechanism for these two effects remains unclear. Here we report features in the electronic structure of $Bi_2Sr_2Ca_2Cu_3O_{10+\delta}$ superconductor that helps to explain this issue. Our angle-resolved photoemission spectroscopy measurements show the splitting of bands from the three layers, and this allows us to parameterize a three-layer interaction model that effectively describes the data. This, in turn, demonstrates the electronic origin of the maximum $T_c$ and its persistence in the overdoped region. These results are qualitatively consistent with a composite picture where a high $T_c$ is realized in an array of coupled planes with different doping levels such that a high pairing strength is derived from the underdoped planes, whereas a large phase stiffness comes from the optimally or overdoped ones.

Although significant progress has been made in experimental and theoretical studies of high-temperature cuprate superconductors, the mechanism of high-temperature superconductivity remains a prominent issue in condensed-matter physics[1,2]. In addition to pinning down on the microscopic origin of electron pairing, the challenge also lies in uncovering the key ingredients that dictate high-temperature superconductivity. It has been found that the doping level is a key controlling parameter in determining the superconducting transition temperature ($T_c$); a maximum $T_c$ can usually be observed at the optimal doping ($p \approx 0.16$). It has also been found that even within the same class of cuprate superconductors, the maximum $T_c$ value sensitively depends on the number of $CuO_2$ planes ($n$) in one structural unit: the maximum $T_c$ increases with $n$ from single layer ($n = 1$) to triple layer ($n = 3$), reaches a maximum at $n = 3$ and starts to decrease with further increase in $n$ (Supplementary Fig. 1a)[3–7]. Moreover, the three-layer $Bi_2Sr_2Ca_2Cu_3O_{10+\delta}$ (Bi2223) superconductor exhibits an unusual phase diagram: its $T_c$ is nearly constant in the optimally and overdoped regions (Supplementary Fig. 1b)[8,9]. This is in strong contrast to the usual phase diagram where $T_c$ decreases with increasing doping in the overdoped region in other one-layer or two-layer cuprate superconductors. Revealing the underlying electronic origin of $T_c$ maximization in trilayer superconductors and its high-$T_c$ persistence in the overdoped region is important in

[1]National Lab for Superconductivity, Beijing National laboratory for Condensed Matter Physics, Institute of Physics, Chinese Academy of Sciences, Beijing, China. [2]University of Chinese Academy of Sciences, Beijing, China. [3]Max Planck Institute for Solid State Research, Stuttgart, Germany. [4]Technical Institute of Physics and Chemistry, Chinese Academy of Sciences, Beijing, China. [5]Songshan Lake Materials Laboratory, Dongguan, China. [6]Beijing National Laboratory for Condensed Matter Physics, Institute of Physics, Chinese Academy of Sciences, Beijing, China. [7]Beijing Academy of Quantum Information Sciences, Beijing, China. [8]These authors contributed equally: Xiangyu Luo, Hao Chen, Yinghao Li. ✉e-mail: XJZhou@iphy.ac.cn
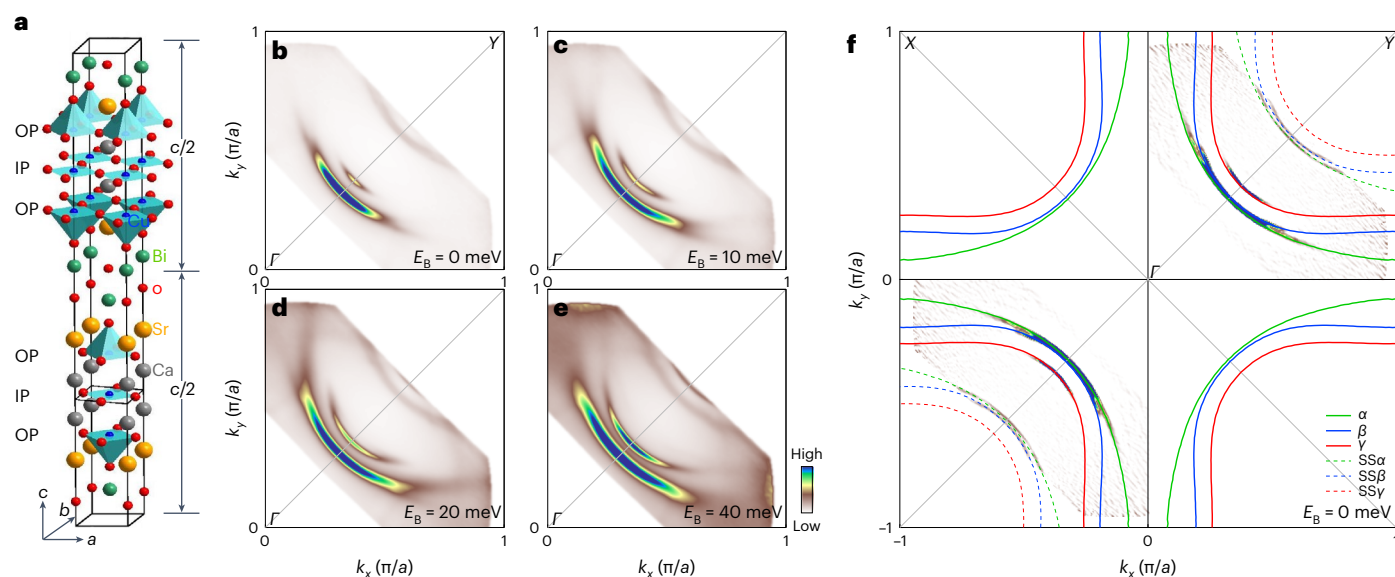
**Fig. 1 | Observation of three Fermi surface sheets in Bi2223. a**, Crystal structure of Bi2223. It consists of two structural units in one unit cell along the $c$ axis, which are displaced with each other by $(a/2, b/2)$. Each structural unit contains three adjacent CuO$_2$ planes with one inner plane (IP) and two outer planes (OPs). **b**–**e**, Fermi surface mapping (**b**) and constant-energy contours at binding energies of 10 meV (**c**), 20 meV (**d**) and 40 meV (**e**) measured at 18 K. **f**, Fermi surface of Bi2223 obtained from the analyses of the Fermi surface mappings in **b**–**e** and related

band structures (Fig. 2). The second-derivative image of **b** is shown in the first and third quadrants. Three Fermi surface sheets are observed, labelled as $\alpha$, $\beta$ and $\gamma$. They are fitted by using a tight-binding model (Supplementary Information) and the fitted curves are plotted as solid lines of green ($\alpha$), blue ($\beta$) and red ($\gamma$) colours. The dashed lines represent the first-order superstructure Fermi surface (SS$\alpha$, SS$\beta$ and SS$\gamma$) caused by the superstructure modulation in Bi2223 with a wavevector of $Q = (0.247, 0.247)\pi/a$.

understanding the superconductivity mechanism and further enhancing $T_c$ in cuprate superconductors.

So far, Bi2223 is the only trilayer superconductor on which extensive angle-resolved photoemission spectroscopy (ARPES) studies have been carried out[10–18]. In Bi2223 with three adjacent CuO$_2$ planes in one structural unit (Fig. 1a), band structure calculations propose that three Fermi surface sheets should arise due to interlayer interactions[19]. However, only one Fermi surface[10–13] or two Fermi surface sheets[14–18] have been observed in all the previous ARPES measurements on Bi2223. The absence of three Fermi surface sheets measured in Bi2223 has been attributed to the charge imbalance between the inner and outer CuO$_2$ planes and the weak interlayer coupling[14,15,17,18].

In this paper, by taking high-resolution laser-based ARPES measurements, we report—for the first time to the best of our knowledge—the observation of three Fermi surface sheets in Bi2223. The momentum dependence of the superconducting gap along all the three Fermi surface sheets is determined and the Bogoliubov band hybridization between two specific bands is observed. These observations make it possible to comprehensively analyse the intralayer and interlayer couplings and pairings. The observed Fermi surface topology, selective band hybridization and unusual Fermi-surface- and momentum-dependent superconducting gap can be well understood by a three-layer interaction model with a global set of parameters. Our results reveal the microscopic origin of the unusual superconducting properties in trilayer superconductors.

The ARPES measurements were carried out on an overdoped Bi2223 sample with a $T_c$ of 108.0 K (Supplementary Fig. 2). Figure 1 shows the Fermi surface mapping and constant-energy contours measured at 18 K. The corresponding band structures along the momentum cuts from the nodal direction to the antinodal region are presented in Fig. 2. From these results, three main Fermi surface sheets (labelled as $\alpha$, $\beta$ and $\gamma$ in Fig. 1f) and three main bands (marked as $\alpha$, $\beta$ and $\gamma$ in Fig. 2) are clearly observed. In the Fermi surface mapping (Fig. 1b), the spectral weight is mainly confined to the nodal region because of the anisotropic gap opening that is large near the antinodal region. On increasing the binding energy, the

spectral weight spreads to the antinodal region in the constant-energy contours (Fig. 1c–e) and the full contours of the three main Fermi surfaces show up clearly. By analysing the Fermi surface mapping and the constant-energy contours in Fig. 1b–e, combined with the analysis of the band structures in Fig. 2, we have quantitatively determined the three main Fermi surface sheets (Fig. 1f). The $\gamma$ Fermi surface is well separated from the $(\alpha, \beta)$ sheets. The splitting between the $\alpha$ and $\beta$ sheets increases from the nodal to the antinodal regions, similar to the bilayer splitting observed in Bi$_2$Sr$_2$CaCu$_2$O$_{8+\delta}$ (Bi2212) (refs. 20–23). The corresponding doping levels of the $\alpha$, $\beta$ and $\gamma$ Fermi surface sheets, determined from their areas, are 0.37, 0.22 and 0.08, respectively.

Figure 2 shows the band structure evolution with momentum going from the nodal direction to the antinodal region. Three main bands are clearly observed, labelled as $\alpha$, $\beta$ and $\gamma$ (Fig. 2a, coloured arrows). Along the nodal direction (Fig. 2a, first panel), the $\gamma$ band is well separated from the $(\alpha, \beta)$ bands. Although splitting between the $\alpha$ and $\beta$ bands is a minimum along the nodal direction, careful analyses indicate that $\alpha$ and $\beta$ band splitting already exists along the nodal direction with $\Delta k_F = 0.011\pi/a$ (Supplementary Fig. 3). The $\alpha$ and $\beta$ band splitting increases with the momentum moving from the nodal to antinodal regions. The $\gamma$ band quickly sinks to high binding energy due to gap opening, accompanied by strong spectral weight suppression when the momentum cut shifts from the nodal direction to the antinodal region. Near the antinodal region, the $\beta$ band becomes dominant, which has a much stronger spectral weight than that of the $\alpha$ and $\gamma$ bands. Although the Bogoliubov band hybridization was observed in Bi2223 before[17,18], one particularly interesting observation in the present case is selective band hybridization. We find that it is the Bogoliubov back-bending band of the $\beta$ band that hybridizes with the $\gamma$ band. Such a band hybridization becomes observable starting from momentum cut 3 (Fig. 2a,c), gets stronger with the momentum moving away from the nodal region, reaches the strongest around momentum cut 6 and then gets weaker with further momentum shifting to the antinodal region. Over the entire momentum space, there is no signature that the $\alpha$ band is involved in the selective Bogoliubov band hybridization.
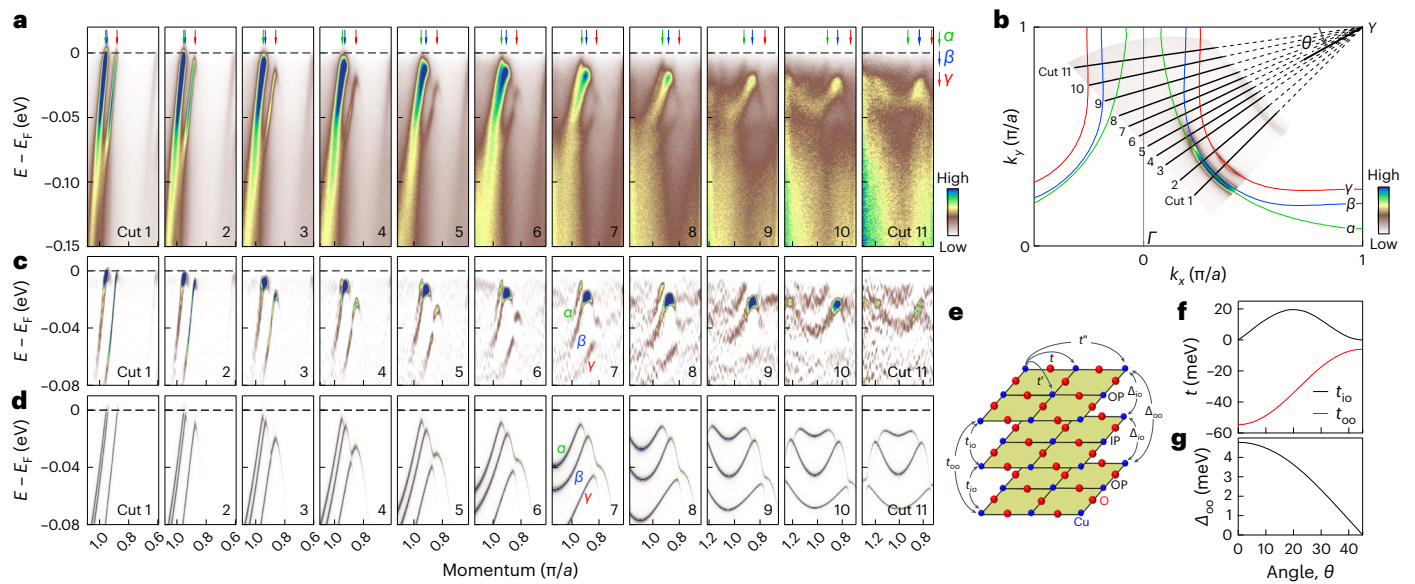
**Fig. 2 | Momentum-dependent band structures of Bi2223 measured at 18 K in the superconducting state and their global simulations. a**, Band structures measured along different momentum cuts. The location of the momentum cuts is shown in **b** as black lines. All of these lines point to the $Y(\pi, \pi)$ point. Three main bands are observed and labelled as $\alpha$, $\beta$ and $\gamma$ and marked by green, blue and red arrows, respectively. The hybridization of the $\beta$ Bogoliubov back-bending band and the $\gamma$ band is clearly observed for the momentum cuts 3–8. **b**, Fermi surface mapping and the simulated three Fermi surface sheets $\alpha$ (green line), $\beta$ (blue line) and $\gamma$ (red line), with the momentum cuts marked. The simulated Fermi surface is in good agreement with the measured Fermi surface. **c**, Corresponding EDC second-derivative images from **a**. **d**, Simulated band structures along the same

momentum cuts as in **b** by the single set of parameters. Supplementary Section 5 provides details of the simulation. **e**, Schematic of the hopping and pairing processes among the three CuO₂ planes. Here $t$, $t'$ and $t''$ represent the in-plane nearest-neighbour, second-nearest-neighbour and third-nearest-neighbour hoppings, respectively. Also, $t_{io}$ represents the interlayer hopping between the inner CuO₂ plane (IP) and the outer planes (OPs), whereas $t_{oo}$ represents interlayer hopping between the two outer planes, $\Delta_{io}$ refers to interlayer pairing between the inner and outer CuO₂ planes and $\Delta_{oo}$ refers to interlayer pairing between the two outer planes. **f,g**, Values of $t_{io}$ (black line) and $t_{oo}$ (red line) (**f**) and interlayer pairing $\Delta_{oo}$ (**g**) used in the global simulation.

To determine the superconducting gap along the three main Fermi surface sheets, we show symmetrized energy distribution curves (EDCs) along the three Fermi surfaces in Fig. 3a–c (Supplementary Fig. 4 shows the original EDCs). The gap size is obtained from the peak position in the symmetrized EDCs. Since the $\alpha$ band is relatively weak, sitting on top of the strong $\beta$ band, it shows up as shoulders in the symmetrized EDCs (Fig. 3a, ticks). The EDC peaks for the $\beta$ band are strong and obvious along the entire Fermi surface (Fig. 3b). For the $\gamma$ band, prominent EDC peaks are observed along the Fermi surface near the nodal region within the Fermi surface angles of $\theta$ = −45–26° and then the two EDC peaks appear near the antinodal region (Fig. 3c). The superconducting gap along the three Fermi surface sheets, obtained from the symmetrized EDCs in Fig. 3a–c, is plotted in Fig. 3d. The $\alpha$, $\beta$ and $\gamma$ Fermi surfaces show fairly different maximum gap sizes of 17, 29 and 62 meV, respectively, near the antinodal region. Their momentum dependence deviates from a simple $d$-wave form of $\Delta = \Delta_0\cos(2\theta)$. There appears a discrete jump for the superconducting gap of the $\gamma$ Fermi surface near the antinodal region, as observed even in Bi2223 before[17,18].

In principle, for a three-CuO₂-layer system (Fig. 2e), the Fermi surface, band structures, superconducting gap and band hybridization can be described by the following full Hamiltonian[18]:

$$H = \phi^\dagger \begin{pmatrix} \epsilon_{op}(k) & t_{io}(k) & t_{oo}(k) & \Delta_{op}(k) & \Delta_{io}(k) & \Delta_{oo}(k) \\ t_{io}(k) & \epsilon_{ip}(k) & t_{io}(k) & \Delta_{io}(k) & \Delta_{ip}(k) & \Delta_{io}(k) \\ t_{oo}(k) & t_{io}(k) & \epsilon_{op}(k) & \Delta_{oo}(k) & \Delta_{io}(k) & \Delta_{op}(k) \\ \Delta_{op}(k) & \Delta_{io}(k) & \Delta_{oo}(k) & -\epsilon_{op}(k) & -t_{io}(k) & -t_{oo}(k) \\ \Delta_{io}(k) & \Delta_{ip}(k) & \Delta_{io}(k) & -t_{io}(k) & -\epsilon_{ip}(k) & -t_{io}(k) \\ \Delta_{oo}(k) & \Delta_{io}(k) & \Delta_{op}(k) & -t_{oo}(k) & -t_{io}(k) & -\epsilon_{op}(k) \end{pmatrix} \phi. \quad (1)$$

Here the bare bands of the inner plane and outer planes, namely, $\epsilon_{ip}(k)$ and $\epsilon_{op}(k)$, respectively, can be described by the tight-binding model (Fig. 2e). The definitions of $t_{io}$, $t_{oo}$, $\Delta_{io}$ and $\Delta_{oo}$ are shown in Fig. 2e. Here $\Delta_{ip}$ denotes the intralayer pairing on the inner plane and $\Delta_{op}$ denotes the intralayer pairing on the outer planes.

Our experimental observations (Figs. 1–3) make it possible to extract all these microscopic parameters. In previous studies of Bi2223 where two Fermi surface sheets are observed[15,17,18], only $t_{io}$ is considered whereas $t_{oo}$ is taken as zero. We started by taking the same approach and tried to fit our data. In this case, a strongly momentum-dependent $t_{io}$ (Supplementary Fig. 6d) must be assumed to get three separated Fermi surface sheets that can well match the measured ones (Supplementary Fig. 6c). However, the simulated band structures (Supplementary Fig. 6a) show obvious discrepancies from the measured ones (Supplementary Fig. 6b). The most notable difference is that in the simulated band structures (Supplementary Fig. 6a), the Bogoliubov band hybridization always occurs between the $\alpha$ and $\gamma$ bands, whereas in the measured results (Supplementary Fig. 6b), the hybridization is actually between the $\beta$ and $\gamma$ bands. In addition, in the simulated band structures (Supplementary Fig. 6a), the Bogoliubov band hybridization dramatically and monotonically increases from the nodal to antinodal regions. But in the measured band structures (Supplementary Fig. 6b), band hybridization is strong in the intermediate range between the nodal and antinodal regions and becomes rather weak near the antinodal region. These results indicate that it is impossible to describe our measured results by only considering $t_{io}$.

Only after $t_{oo}$ is taken into account, the observed Fermi surface, band structure, superconducting gap and Bogoliubov band hybridization can be well described (Fig. 2b,d). In this case, a strongly anisotropic $t_{oo}(k) = t_{oo0} + t_{oo1}(\cos(k_xa) - \cos(k_ya))^2/4$ is assumed with $t_{oo0} = -6.0$ meV and $t_{oo1} = -53.3$ meV (Fig. 2f, red line). It is even stronger than $t_{io}$ (Fig. 2f,
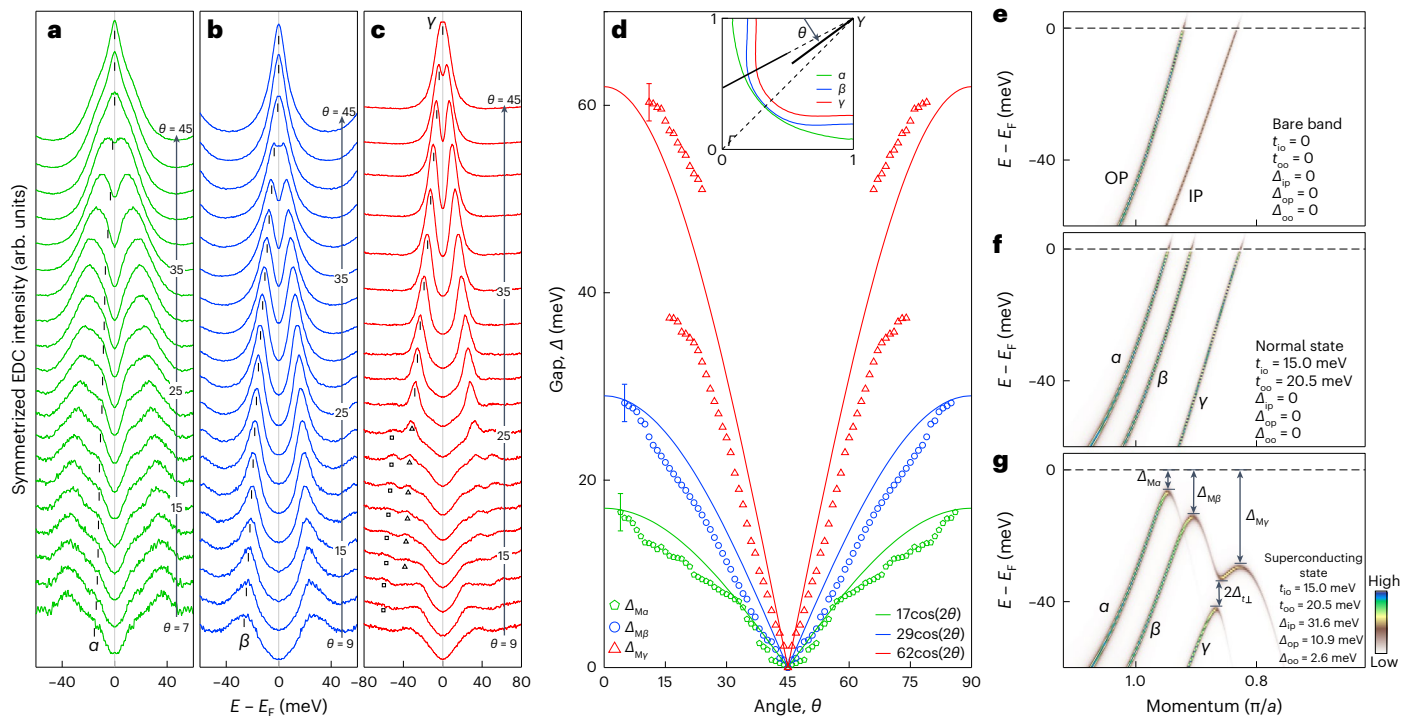
**Fig. 3 | Photoemission spectra and the superconducting gap of Bi2223 along the three Fermi surface sheets measured at 18 K. a–c,** Symmetrized EDCs along the $\alpha$ (**a**), $\beta$ (**b**) and $\gamma$ (**c**) Fermi surface sheets. The location of the Fermi momentum is defined by angle $\theta$, as shown in the inset of **d**. The symmetrized EDC peaks that correspond to the $\alpha$ band are marked by ticks in **a**; they are on the shoulders of the symmetrized EDC peaks of the underlying $\beta$ band. The symmetrized EDC peaks that correspond to the $\beta$ band are marked by ticks in **b**. For the symmetrized EDCs along the $\gamma$ Fermi surface, one main peak is observed near the nodal region with $\theta = -45-27°$, as marked by the ticks in **c**. Towards the antinodal region with $\theta = -25-15°$, two EDC peaks are observed due to band hybridization, as marked by triangles and squares in **c**. **d,** Superconducting gaps along the three Fermi surface sheets obtained from the symmetrized EDCs in

**a–c.** The uncertainty is ±2 meV, as marked on the leftmost points. For comparison with the standard d-wave form of $\Delta = \Delta_0\cos(2\theta)$, three lines are plotted for the $\alpha$, $\beta$ and $\gamma$ Fermi surfaces with $\Delta_0$ of 17 meV (green line), 29 meV (blue line) and 62 meV (red line). **e–g,** Simulated band structures along a momentum cut in the normal and superconducting states. The location of the momentum cut is shown in the inset of **d** as a black line. **e,** Bare bands of the inner plane (IP) and outer plane (OP). **f,** Three bands that are produced after the introduction of the interlayer couplings of $t_{io}$ and $t_{oo}$. **g,** Band structures in the superconducting state when the interlayer pairing between the two outer planes, $\Delta_{oo}$, is added on top of $\Delta_{ip}$ and $\Delta_{op}$. The hybridization gap $2\Delta_{t\perp}$ is also defined. Note that the Fermi momentum of the three bands remains fixed from the normal state in **f** to the superconducting state in **g**.

black line). This $t_{oo}$ value mainly determines band splitting between the $\alpha$ and $\beta$ bands, as seen from the diagonalized Hamiltonian (Supplementary Equation (8)). Here $t_{oo1}$ is responsible for the slight band splitting along the nodal direction, whereas the increase in band splitting from the nodal to antinodal regions originates from the $t_{oo1}$ term. It is interesting to note that $t_{oo}$ has the opposite sign to that of $t_{io}$ (Fig. 2f). After considering $t_{oo}$, the Bogoliubov band hybridization occurs between the $\beta$ and $\gamma$ bands (Fig. 2d), which becomes consistent with the measured results (Fig. 2a,c). We note that $t_{oo}$ mainly dictates band splitting between the $\alpha$ and $\beta$ bands, whereas $t_{io}$ plays a dominant role in the Bogoliubov band hybridization.

The proper considerations of $t_{io}$ and $t_{oo}$ have set a good stage to describe the Fermi surface and band structures of Bi2223 in the normal state. To understand its superconducting state, the intralayer gaps of the inner plane ($\Delta_{ip}$) and outer planes ($\Delta_{op}$) are usually considered[17,18]. With the discovery of three Fermi surface sheets, particularly the notably different superconducting gaps between the $\alpha$ and $\beta$ Fermi surfaces (Fig. 3d), we find that the inclusions of $\Delta_{ip}$ and $\Delta_{op}$ alone cannot properly describe the observed superconducting gap structure because, in this case, the gap difference between the $\alpha$ and $\beta$ Fermi surfaces is always small (Supplementary Fig. 7h), which is much smaller than the observed gap difference near the antinodal region. To overcome such a discrepancy, $\Delta_{oo}$ has to be considered. After considering $\Delta_{oo}$, which takes a d-wave form of $\Delta_{oo} = 5\cos(2\theta)$ (Fig. 2g), the simulated gap structure becomes consistent with the measured one (Supplementary

Figs. 7p and 8). We note that $\Delta_{io}$ is negligible compared with $\Delta_{oo}$. First, the inclusion of $\Delta_{io}$ reduces the gap size of the $\beta$ band and further reduces the gap difference between the $\alpha$ and $\beta$ bands (Supplementary Fig. 7k,l), which goes against the experimental results. Second, if $\Delta_{io}$ is significant and takes a d-wave form, it will enhance the Bogoliubov band hybridization near the antinodal region, which is not consistent with the measured result that the hybridization is weak near the antinodal region (Fig. 2a,c).

The above discussions result in the three-layer Hamiltonian (Supplementary Equation (7)) that—when the related parameters are properly taken (Fig. 2f,g)—can satisfactorily describe the observed Fermi surface (Fig. 2b), band structures, superconducting gaps and Bogoliubov band hybridizations (Fig. 2d). Further diagonalization of the Hamiltonian (Supplementary Equation (8)) indicates that the Bogoliubov band hybridization occurs only between the $\beta$ and $\gamma$ bands but not affected by the $\alpha$ band. This makes it possible to fit the observed $\beta$ and $\gamma$ bands and quantitatively extract the related parameters (Supplementary Equations (10)–(12)). Figure 4b shows the fitted results of the $\beta$ and $\gamma$ bands; Supplementary Figs. 9 and 10 provide the detailed fittings of more momentum cuts. From the fittings, the hybridization gap $2\Delta_{t\perp}$ (Fig. 3g) is obtained and plotted in Fig. 4c. It exhibits a non-monotonic momentum dependence that the band hybridization is strong in the intermediate region within $\theta = -15-39°$ but becomes rather weak near the nodal and antinodal regions. Similarly, the extracted $t_{io}$ (Fig. 4d) is also non-monotonic, which is strong in the intermediate region
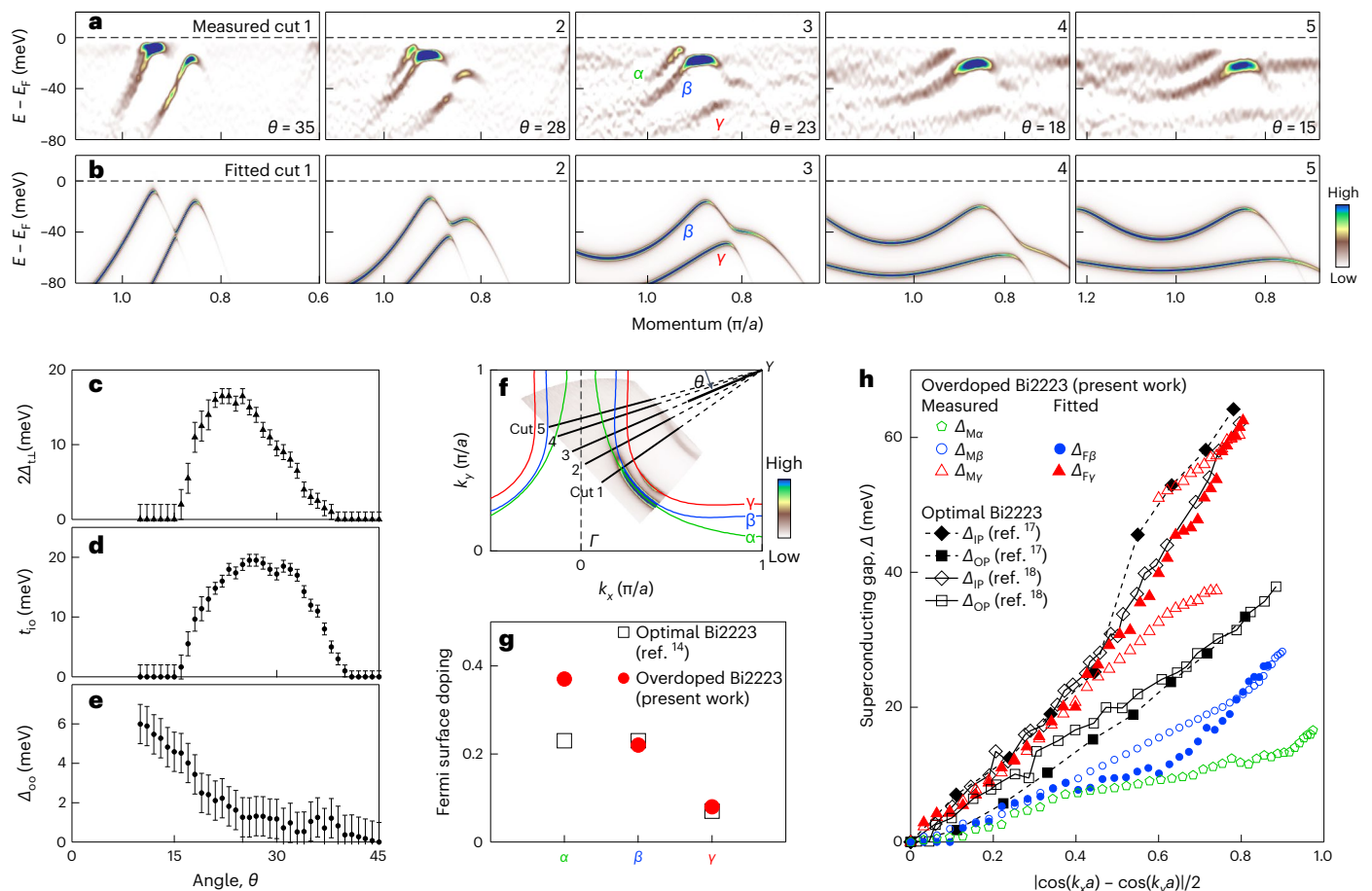
**Fig. 4 | Determination of interlayer hopping, interlayer pairing and band hybridization parameters in Bi2223. a**, Band structures measured along five typical momentum cuts. The location of the momentum cuts is marked by the black lines in **f**. These are EDC second-derivative images, which can show the band hybridization between $\beta$ and $\gamma$ bands more clearly. **b**, Fitted band structures along the same five momentum cuts as in **a** by considering the band hybridization of the $\beta$ and $\gamma$ bands. Supplementary Section 9 provides the fitting details. **c,d**, Hybridization gap $2\Delta_{L\perp}$ (**c**) and interlayer hopping $t_{io}$ (**d**) as a function of angle $\theta$ extracted from fitting the band hybridizations in **a** (**b** and Supplementary Figs. 9 and 10). The uncertainties are ±1 meV with $\theta$ = ~45–21° and ±2 meV with $\theta$ = ~21–10° as marked by the error bars. **e**, Interlayer pairing $\Delta_{oo}$ obtained from

the superconducting gaps along the $\alpha$ and $\beta$ Fermi surface sheets shown in **h**. The uncertainties are ±1 meV as marked by the error bars. **f**, Fermi surface of Bi2223 and the location of momentum cuts. **g**, Doping levels corresponding to the Fermi surface sheets in our overdoped Bi2223 (red solid circles) and in the optimally doped Bi2223 (black empty squares)[14]. **h**, Superconducting gaps as a function of $|\cos(k_xa) - \cos(k_ya)|/2$ along the three Fermi surfaces in our overdoped Bi2223 (Fig. 3d). The fitted superconducting gaps along the $\beta$ ($\Delta_{F\beta}$, solid blue circles) and $\gamma$ ($\Delta_{F\gamma}$, solid red triangles) Fermi surface sheets extracted from the band structure fitting in **b** and Supplementary Figs. 9 and 10 are included. For comparison, the superconducting gaps measured in the optimally doped Bi2223 (refs. 17,18) are also plotted.

within $\theta$ = ~15–39° but gets rather weak near the nodal and antinodal regions. When the momentum moves from the nodal region to the antinodal region, the signal-to-noise ratio in the data gets worse and the $\gamma$ band near the antinodal region becomes rather weak in the data. However, Supplementary Fig. 10 shows that the hybridization gap gradually decreases from a finite value for $\theta$ = 20° to nearly zero for $\theta$ = 15°. The fitting-extracted bare superconducting gaps of the $\beta$ and $\gamma$ Fermi surfaces, namely, $\Delta_{F\beta}$ and $\Delta_{F\gamma}$, respectively, are plotted in Fig. 4h. They show obvious difference from the measured superconducting gaps in the region of strong band hybridization. In particular, the fitted gap of the $\gamma$ band ($\Delta_{F\gamma}$) is monotonic and continuous, which is different from the observed gap jump due to strong Bogoliubov band hybridization. As evident from the diagonalized Hamiltonian (Supplementary Equation (8)), the fitted gap of the $\beta$ band ($\Delta_{F\beta}$) corresponds to $\Delta_{op} + \Delta_{oo}$, whereas the measured gap of the $\alpha$ band corresponds to $\Delta_{op} - \Delta_{oo}$. Therefore, $\Delta_{oo}$ can be directly extracted from the gap difference $2\Delta_{oo} = \Delta_{F\beta} - \Delta_{M\alpha}$ (Fig. 4e). The experimentally extracted $t_{io}$ (Fig. 4d) and $\Delta_{oo}$ (Fig. 4e) are consistent with those used in the global simulation (Fig. 2f,g).

We find that the interlayer hoppings in the overdoped Bi2223 measured here are fairly unusual. First, interlayer hopping $t_{io}$ exhibits an unusual momentum dependence. Usually, this term is assumed to monotonically increase from the nodal to antinodal regions[17,18]. However, the measured $t_{io}$ is non-monotonic and gets strongly suppressed near the antinodal region (Fig. 4d). One possibility is that this may be caused by intercell hopping. In Bi2223, one cell consists of three $CuO_2$ planes and one unit cell contains two cells that are shifted by $(a/2, b/2)$ (Fig. 1a). Whether the intercell hopping may give rise to such an unusual $t_{io}$ needs further investigations[24]. In another Bi-based superconductor Bi2212, it has been shown that the single cell can embody the same physical properties as the bulk[25]. The other possibility is that such an unusual $t_{io}$ is intrinsic to the single cell of three $CuO_2$ layers, which has uneven charge distribution and the inner plane is heavily underdoped with pseudogap formation near the antinodal region. More efforts are also needed to pin down the effect of pseudogap formation on the unusual $t_{io}$ in Bi2223.

The second unusual behaviour of the interlayer hoppings is that $t_{oo}$ is large and even stronger than $t_{io}$. Usually, $t_{oo}$ is assumed to be zero

in Bi2223 because the distance between the two outer planes is twice that between the inner and outer planes[17,18]. The enhancement in $t_{oo}$ in the overdoped Bi2223 studied here may be related to the increased doping levels on the outer $CuO_2$ planes. In multilayer cuprates, the interlayer hopping is realized via the Cu3$dz^2$ and Cu4$s$ orbitals[26]. There is experimental evidence of a strong increase in interlayer hopping with increasing doping in Bi2212 (ref. 27). It has been shown that in multilayer systems, interlayer hopping depends not only on the distance between the layers but also on the doping levels on each layer[28].

To understand the $T_c$ maximum in trilayer cuprate superconductors, two main ideas have been proposed. The first is related to the interlayer pair hopping that may enhance superconductivity[4,29]. The second is a composite picture where a high pairing scale is derived from the underdoped planes and a large phase stiffness from the optimally or overdoped ones[30–32]. Our results are qualitatively consistent with the composite picture[30–32]. For superconductors with a low superfluid density like cuprate superconductors, it has been shown that $T_c$ is determined not only by the pairing strength but also by the phase coherence[33]. When there is only one $CuO_2$ plane in a cell like in $Bi_2Sr_2CuO_{6+\delta}$ (Bi2201) or there are two equivalent $CuO_2$ planes in a cell like in Bi2212, the pairing strength and phase coherence have to be realized on the same $CuO_2$ plane that makes them difficult to be optimized. But in Bi2223, there are two kinds of distinct $CuO_2$ plane that makes it possible to separately optimize the pairing strength and phase coherence on different planes. The $\gamma$ Fermi surface mainly originates from the inner plane. It is heavily underdoped ($p \approx 0.08$) with a large superconducting gap (Fig. 4h), which may act as the source of strong pairing strength. The $\alpha$ and $\beta$ Fermi surfaces mainly come from the two outer $CuO_2$ planes. These two planes are heavily overdoped ($p \approx 0.30$) and may act as a source of strong phase stiffness. On the other hand, it has been found that superconductivity in cuprates is closely related to the superfluid density, as shown for the underdoped and optimally doped region[34] and for the overdoped region[35]. The previous ARPES measurements found that the intensity of the superconducting coherence peak near the antinodal region scales with the superfluid density[36,37]. Looking at the photoemission spectra along the three Fermi surface sheets in Fig. 3a–c and Supplementary Fig. 4, we find that the superconducting coherence peaks in the EDCs near the antinodal region along the $\alpha$ and $\gamma$ Fermi surfaces are weak, whereas they are rather sharp and strong in the EDCs along the $\beta$ Fermi surface. These indicate that the $\beta$ Fermi surface corresponds to a much higher superfluid density than that of the $\alpha$ Fermi surface. Therefore, although both $\alpha$ and $\beta$ Fermi surfaces have high doping levels, it is the $\beta$ Fermi surface that has a high superfluid density and mainly dictates superconductivity. In the real space, the composite structure of a heavily underdoped inner $CuO_2$ plane ($p \approx 0.08$) sandwiched in between two heavily overdoped outer planes ($p \approx 0.30$) helps in achieving high-temperature superconductivity that no individual $CuO_2$ plane can reach. In the reciprocal space, the heavily underdoped $\gamma$ Fermi surface ($p \approx 0.08$) with a large superconducting gap and the overdoped $\beta$ Fermi surface ($p \approx 0.22$) with strong coherence peaks work together to achieve high $T_c$ in Bi2223.

In a composite system, interlayer hopping ($t_\perp$) plays an important role in realizing superconductivity: the maximum $T_c$ can be reached only for an optimized $t_\perp$ (ref. 31). Our extraction of the interlayer hoppings, namely, $t_{io}$ (Fig. 4d) and $t_{oo}$ (Fig. 2f), provides key information to understand high $T_c$ in Bi2223. In our overdoped Bi2223, interlayer hopping $t_{io}$ is slightly larger than that in the optimally doped Bi2223 (ref. 18), whereas $t_{oo}$ is significantly enhanced compared with the negligible value in the optimally doped Bi2223 (ref. 18). These results indicate that among $t_{io}$ and $t_{oo}$, $t_{io}$ plays a more important role in reaching the maximum $T_c$ in Bi2223.

Interlayer hopping $t_{oo}$ plays a key role in maintaining a high $T_c$ in the overdoped Bi2223. In the optimally doped Bi2223, the doping levels of the $\alpha$, $\beta$ and $\gamma$ Fermi surfaces are 0.23, 0.23 and 0.07, with no observable band splitting between the $\alpha$ and $\beta$ bands[14,17,18]. In our overdoped

Bi2223, the doping levels of the $\alpha$, $\beta$ and $\gamma$ Fermi surfaces are 0.37, 0.22 and 0.08. It becomes immediately clear that although the average doping increases from 0.18 to 0.22, the extra doping mainly goes to the $\alpha$ Fermi surface, leaving the doping of the $\beta$ and $\gamma$ Fermi surfaces nearly unchanged in the overdoped Bi2223 (Fig. 4g). These results indicate that with the increase in hole doping from the optimally doped to overdoped Bi2223, the extra holes mainly go to the outer $CuO_2$ planes. Furthermore, due to the $\alpha$ and $\beta$ band splitting from interlayer hopping $t_{oo}$, the extra holes are predominantly absorbed into the $\alpha$ Fermi surface. The $\beta$ Fermi surface mainly controls the phase stiffness and its doping changes little in the optimally doped and overdoped Bi2223 (Fig. 4g). The $\gamma$ Fermi surface mainly controls the pairing strength and its doping level (Fig. 4g) and the superconducting gap (Fig. 4h) shows little change in the optimally doped and overdoped Bi2223. It is, therefore, natural to understand that $T_c$ exhibits a weak doping dependence in the optimally doped and overdoped Bi2223 samples (Supplementary Fig. 1b). In the meantime, the emergence of the interlayer pairing $\Delta_{oo}$ in the overdoped Bi2223 (Fig. 4e) leads to an enhancement in the superconducting gap for the $\beta$ Fermi surface ($\Delta_{M\beta} = \Delta_{op} + \Delta_{oo}$) (Fig. 4h). This, in turn, will also help in maintaining high $T_c$ in the overdoped Bi2223 samples.

## Online content

Any methods, additional references, Nature Portfolio reporting summaries, source data, extended data, supplementary information, acknowledgements, peer review information; details of author contributions and competing interests; and statements of data and code availability are available at https://doi.org/10.1038/s41567-023-02206-0.

## References

1. Lee, P. A., Nagaosa, N. & Wen, X. G. Doping a Mott insulator: physics of high-temperature superconductivity. *Rev. Mod. Phys.* **78**, 17 (2006).
2. Keimer, B., Kivelson, S. A., Norman, M. R., Uchida, S. & Zaanen, J. From quantum matter to high-temperature superconductivity in copper oxides. *Nature* **518**, 179–186 (2015).
3. Scott, B. A. et al. Layer dependence of the superconducting transition temperature of $HgBa_2Ca_{n-1}Cu_nO_{2n+2+\delta}$. *Phys. C* **230**, 239–245 (1994).
4. Chakravarty, S., Kee, H.-Y. & Volker, K. An explanation for a universality of transition temperatures in families of copper oxide superconductors. *Nature* **428**, 53–55 (2004).
5. Iyo, A. et al. $T_c$ vs $n$ relationship for multilayered high-$T_c$ superconductors. *J. Phys. Soc. Jpn* **76**, 094711 (2007).
6. Eisaki, H. et al. Effect of chemical inhomogeneity in bismuth-based copper oxide superconductors. *Phys. Rev. B* **69**, 064512 (2004).
7. Chu, C. W., Deng, L. Z. & Lv, B. Hole-doped cuprate high temperature superconductors. *Phys. C* **514**, 290–313 (2015).
8. Fujii, T., Terasaki, I., Watanabe, T. & Matsuda, A. Doping dependence of anisotropic resistivities in the trilayered superconductor $Bi_2Sr_2Ca_2Cu_3O_{10+\delta}$. *Phys. Rev. B* **66**, 024507 (2002).
9. Piriou, A., Fasano, Y., Giannini, E. & Fischer, Ø. Effect of oxygen-doping on $Bi_2Sr_2Ca_2Cu_3O_{10+\delta}$ vortex matter: crossover from electromagnetic to Josephson interlayer coupling. *Phys. Rev. B* **77**, 184508 (2008).
10. Muller, R. et al. Fermi surface and superconducting gap of triple-layered $Bi_2Sr_2Ca_2Cu_3O_{10+\delta}$. *J. Supercond.* **15**, 147–152 (2002).
11. Feng, D. L. et al. Electronic structure of the trilayer cuprate superconductor $Bi_2Sr_2Ca_2Cu_3O_{10+\delta}$. *Phys. Rev. Lett.* **88**, 107001 (2002).
12. Sato, T. et al. Low energy excitation and scaling in $Bi_2Sr_2Ca_{n-1}Cu_nO_{2n+4}$ ($n$=1–3): angle-resolved photoemission spectroscopy. *Phys. Rev. Lett.* **89**, 067005 (2002).

13. Matsui, H. et al. BCS-like Bogoliubov quasiparticles in high-$T_c$ superconductors observed by angle-resolved photoemission spectroscopy. *Phys. Rev. Lett.* **90**, 217002 (2003).

14. Ideta, S. et al. Enhanced superconducting gaps in the trilayer high-temperature $Bi_2Sr_2Ca_2Cu_3O_{10+\delta}$ cuprate superconductor. *Phys. Rev. Lett.* **104**, 227001 (2010).

15. Ideta, S. et al. Angle-resolved photoemission study of the tri-layer high-$T_c$ superconductor $Bi_2Sr_2Ca_2Cu_3O_{10+\delta}$: effects of inter-layer hopping. *Phys. C* **470**, S14 (2010).

16. Ideta, S. et al. Energy scale directly related to superconductivity in high-$T_c$ cuprates: universality from the temperature-dependent angle-resolved photoemission of $Bi_2Sr_2Ca_2Cu_3O_{10+\delta}$. *Phys. Rev. B* **85**, 104515 (2012).

17. Kunisada, S. et al. Observation of Bogoliubov band hybridization in the optimally doped trilayer $Bi_2Sr_2Ca_2Cu_3O_{10+\delta}$. *Phys. Rev. Lett.* **119**, 217001 (2017).

18. Ideta, S. et al. Hybridization of Bogoliubov quasiparticles between adjacent $CuO_2$ layers in the triple-layer cuprate $Bi_2Sr_2Ca_2Cu_3O_{10+\delta}$ studied by angle-resolved photoemission spectroscopy. *Phys. Rev. Lett.* **127**, 217004 (2021).

19. Camargo-Martínez, J. A., Espitia, D. & Baquero, R. First-principles study of electronic structure of $Bi_2Sr_2Ca_2Cu_3O_{10}$. *Rev. Mex. Fis.* **60**, 39–45 (2014).

20. Feng, D. L. et al. Bilayer splitting in the electronic structure of heavily overdoped $Bi_2Sr_2CaCu_2O_{8+\delta}$. *Phys. Rev. Lett.* **86**, 5550 (2001).

21. Chuang, Y.-D. et al. Doubling of the bands in overdoped $Bi_2Sr_2CaCu_2O_{8+\delta}$: evidence for *c*-axis bilayer coupling. *Phys. Rev. Lett.* **87**, 117002 (2001).

22. Bogdanov, P. V. et al. Photoemission study of Pb doped $Bi_2Sr_2CaCu_2O_{8+\delta}$: a Fermi surface picture. *Phys. Rev. B* **64**, 180505(R) (2001).

23. Ai, P. et al. Distinct superconducting gap on two bilayer-split Fermi surface sheets in $Bi_2Sr_2CaCu_2O_{8+\delta}$ superconductor. *Chinese Phys. Lett.* **36**, 067402 (2019).

24. Markiewicz, R. S., Sahrakorpi, S., Lindroos, M., Lin, H. & Bansil, A. One-band tight-binding model parametrization of the high-$T_c$ cuprates including the effect of $k_z$ dispersion. *Phys. Rev. B* **72**, 054519 (2005).

25. Yu, Y. J. et al. High-temperature superconductivity in monolayer $Bi_2Sr_2CaCu_2O_{8+\delta}$. *Nature* **575**, 156 (2019).

26. Pavarini, E., Dasgupta, I., Dasgupta, T. S., Jepsen, O. & Andersen, O. K. Band-structure trend in hole-doped cuprates and correlation with $T_{cmax}$. *Phys. Rev. Lett.* **87**, 047003 (2001).

27. Zhong, Y. G. et al. Extraction of tight binding parameters from in-situ ARPES on the continuously doped surface of cuprates. *Sci. China Phys. Mech. Astron.* **61**, 127403 (2018).

28. Mori, M., Tohyama, T. & Maekawa, S. Fermi surface splittings in multilayered high-$T_c$ cuprates. *Phys. C* **445**, 23–25 (2006).

29. Nishiguchi, K., Kuroki, K., Arita, R., Oka, T. & Aoki, H. Superconductivity assisted by interlayer pair hopping in multilayered cuprates. *Phys. Rev. B* **88**, 014509 (2013).

30. Kivelson, S. A. Making high $T_c$ higher: a theoretical proposal. *Phys. B* **318**, 61–67 (2002).

31. Berg, E., Orgad, D. & A. Kivelson, S. Route to high-temperature superconductivity in composite systems. *Phys. Rev. B* **78**, 094509 (2008).

32. Okamoto, S. & Maier, T. A. Enhanced superconductivity in superlattices of high-$T_c$ cuprates. *Phys. Rev. Lett.* **101**, 156401 (2008).

33. Emery, V. J. & Kivelson, S. A. Importance of phase fluctuations in superconductors with small superfluid density. *Nature* **374**, 434–437 (1995).

34. Uemura, Y. J. et al. Universal correlations between $T_c$ and $n_s/m^*$ (carrier density over effective mass) in high-$T_c$ cuprate superconductors. *Phys. Rev. Lett.* **62**, 2317 (1989).

35. Božović, I., He, X., Wu, J. & Bollinger, A. T. Dependence of the critical temperature in overdoped copper oxides on superfluid density. *Nature* **536**, 309–311 (2016).

36. Feng, D. L. et al. Signature of superfluid density in the single-particle excitation spectrum of $Bi_2Sr_2CaCu_2O_{8+\delta}$. *Science* **289**, 277–281 (2000).

37. Ding, H. et al. Coherent quasiparticle weight and its connection to high-$T_c$ superconductivity from angle-resolved photoemission. *Phys. Rev. Lett.* **87**, 227001 (2001).

## Methods

High-quality single crystals of Bi2223 were grown by the travelling-solvent floating zone method[38]. The samples were post-annealed at 550 °C under a high oxygen pressure of about 170 atmospheres for 7 days. The obtained samples are overdoped with a $T_c$ of 108.0 K and a transition width of $\Delta T \approx 3.0$ K (Supplementary Fig. 2).

ARPES measurements were carried out using our lab-based laser ARPES systems equipped with a 6.994 eV vacuum-ultraviolet laser and a DA30L hemispherical electron energy analyser[39,40]. The energy resolution was set at 1 meV and the angular resolution is approximately 0.3°, corresponding to a momentum resolution of 0.004 Å$^{-1}$. All the samples were cleaved in situ at a low temperature and measured in a vacuum with a base pressure better than $5 \times 10^{-11}$ torr at 18 K. The Fermi level is referenced by measuring on clean polycrystalline gold that is electrically connected to the sample.

## Data availability

All raw data generated during the study are available from the corresponding author upon request.

## Code availability

The codes used for the fitting and simulation process in this study are available from the corresponding author upon request.

## References

38. Liang, B., Lin, C. T., Shang, P. & Yang, G. Single crystals of triple-layered cuprates Bi$_2$Sr$_2$Ca$_2$Cu$_3$O$_{10+\delta}$: growth, annealing and characterization. *Phys. C* **383**, 75–88 (2002).
39. Liu, G. D. et al. Development of a vacuum ultraviolet laser-based angle-resolved photoemission system with a superhigh energy resolution better than 1meV. *Rev. Sci. Instrum.* **79**, 023105 (2008).
40. Zhou, X. J. et al. New developments in laser-based photoemission spectroscopy and its scientific applications: a key issues review. *Rep. Prog. Phys.* **81**, 062101 (2018).

## Author contributions

X.J.Z. and X.L. proposed and designed the research. X.L., H.C., C.Y., Q.G. and H.Y. carried out the ARPES experiments. C.L. grew the single crystals. H.C., C.Y., T.M., H.L., Y.S., Y.C., S.Z., Z.W., F.Z., F.Y., Q.P., G.L., L.Z., Z.X. and X.J.Z. contributed to the development and maintenance of the laser ARPES and ARTOF systems. X.L., Y.L., Q.G. and T.X. contributed to the theoretical analysis. X.L. and X.J.Z. analysed the data and wrote the paper. All authors participated in the discussions and commented on the paper.

## Competing interests

The authors declare no competing interests.

## Additional information

**Supplementary information** The online version contains supplementary material available at https://doi.org/10.1038/s41567-023-02206-0.

**Correspondence and requests for materials** should be addressed to X. J. Zhou.

**Peer review information** *Nature Physics* thanks Robert Markiewicz and the other, anonymous, reviewer(s) for their contribution to the peer review of this work.

**Reprints and permissions information** is available at www.nature.com/reprints.